# Slip analysis in a Ni-base superalloy

Eboni F. Westbrooke, Luis E. Forero and Fereshteh Ebrahimi*

Materials Science and Engineering Department

University of Florida, P.O. Box 116400, Gainesville, FL 32611

* Corresponding author, email: febra@mse.ufl.edu

## Abstract

A Ni-base superalloy single crystal with $\gamma/\gamma'$ structure was tested at room temperature along the <100>, <110> and <111> directions. Consistent with previously reported investigations, this alloy did not obey the Schmid law and the CRSS (critical resolved shear stress) was noticeably lower for the <111>-oriented samples. Furthermore, the strain hardening rate decreased and the degree of deformation localization increased in the order of <111>, <100> and <110> orientations. The appearance and orientation of deformation traces were found to depend on the loading orientation as well as the amount of strain. In general, when $\gamma'$-particles were sheared, the traces followed the expected octahedral shear planes. It is demonstrated that the wavy deformation traces that do not follow the {111} planes are associated with changes in the $\gamma$-channels width and the falling off of the $\gamma'$-particles. In this paper the evolution of deformation bands are discussed in terms of plastic localization at microscopic, mesoscopic and macroscopic levels.

## 1. Introduction

Nickel-base superalloys are the main materials in use for the production of blades employed in gas turbines, power generators, and aircraft engines. The microstructure of these alloys consists of ordered $\gamma$'-precipitates ($L1_2$ structure) coherently set in a face centered cubic (FCC) nickel-base solid solution $\gamma$-matrix. In the majority of Ni-base superalloys, the precipitates are cubical in shape with their faces parallel to the {100} planes. The size of the $\gamma$'-cubes as well as the $\gamma$-channels left in between them is in the sub-micrometer regime. The plastic deformation of the $\gamma/\gamma$' microstructure can be quite complex and the contribution of each phase to the deformation process depends on many parameters including the composition, volume fraction and size of the precipitates, the $\gamma/\gamma$' interfacial composition and structure, crystallographic orientation, temperature and strain rate [1-4].

Plastic deformation of $L1_2$ type structures transpires by motion of super-lattice dislocations on {111} planes at low temperatures, whereas at higher temperatures the dominant slip planes change from {111} to {100} [5]. When a non-superdislocation (super dislocation b = a<110>) shears an $L1_2$ lattice an anti-phase boundary (APB) is produced. Since the anti-phase boundary energy (APBE) on the {100} planes is lower than that on the {111} planes, it becomes energetically favorable for dislocation pairs to lie on the {100} planes rather than on the {111} planes. However, due to the low mobility of dislocations on the {100} planes, they become pinned after cross-slipping from the {111} planes. Increasing the temperature assists the motion of the dislocations on {100} planes, and hence the predominant slip planes change from the {111} to the {100} planes [6]. The increase in the probability of dislocation cross-slip is believed to be

responsible for the observation of a peak in the critical resolved shear stress (CRSS) of the $\gamma$'-phase as a function of temperature. It has been shown that owing to the orientation dependency of the cross-slip process, the $\gamma$'-phase does not follow Schmid law, i.e. the CRSS is not the same on all equivalent slip systems [7].

The deformation of the $\gamma$-matrix depends on the level of supersaturation (or formation of clusters) and the width of the channels, which controls the dislocation bowing stress [8]. If the stress needed to bow dislocations within the $\gamma$-channels is smaller than that needed to generate dislocations in the $\gamma$' precipitates, then the plastic deformation of the $\gamma/\gamma$' microstructure proceeds by the motion of dislocations within the $\gamma$-channels, their accumulation at the $\gamma/\gamma$' interface and finally their penetration into the $\gamma$'-precipitates (shearing of the precipitates). Increasing the channel size or temperature (below the peak temperature) facilitates this deformation mechanism by reducing the stress needed to move the dislocations within the channels and increasing the stress needed to yield the $\gamma$'-precipitate, respectively. At low-test temperatures, e.g. room temperature, and high volume fractions of small $\gamma$' precipitates, plastic deformation has been suggested to begin in the $\gamma$'-phase [9]. Several studies have demonstrated that the break down of Schmid law is a characteristic feature not only for the $\gamma$'-phase with the $L1_2$ structure, but also for all superalloys containing a high, medium or even low volume fraction of the $\gamma$'-phase [10,11]. It has been shown that the degree of anisotropy depends on the test temperature as well as the size and shape of the $\gamma$'-precipitates [2,12] The yielding anisotropy of the superalloys has been attributed to the non-Schmid effect of the $\gamma$'-precipitates [13]. However, it is not clear why in the case where yielding occurs by the

expansion of dislocations in the γ-channels, the superalloy does not follow Schmid law, since the cross-slip of super dislocations to the {100} planes is not applicable to the FCC matrix.

The activation of slip planes can be investigated by studying the slip traces on the tensile (or compression) samples and by observing thin foils of deformed samples in the transmission electron microscope (TEM). A few studies have demonstrated that for samples loaded near the <111> orientation, the apparent slip bands follow the {100} traces [2,13,14]. However, detailed TEM analysis has revealed that at low deformation temperatures, despite the macroscopic observation, the slip had occurred on the {111} planes within the γ-channels in a zig-zag configuration as a result of dislocation cross-slip among the activated {111} slip planes [14]. The macroscopic {100} slip traces have been attributed to a "linked" gliding mechanism, where wide channels provide free paths for dislocation motion. It has been discussed [11] that this mechanism is not operable in samples loaded along a <110> orientation because of lack of cross-slip possibility. In the case of <100>-oriented samples, it is argued [11] that the resolved shear stresses press the dislocations against the γ/γ' interface rather than driving them to the opposite parallel interface, which is necessary for the "linked" gliding mechanism. However, it is not clear what factors govern the apparent macroscopic slip traces in samples loaded in directions other than a <111> direction.

The purpose of this investigation was to study the non-Schmid behavior and the evolution of apparent macroscopic slip bands in a Ni-base superalloy with a relatively wide γ-channel as a function of crystallographic orientation at room temperature.

## 2. Experimental Procedures

A Ni-base superalloy cast in slab dimensions of 17.6 X 74 X 155 mm was provided by Pratt and Whitney in the heat-treated condition. Examination of the alloy by scanning electron microscopy (SEM), as shown in Figure 1, indicated a volume fraction of cubical γ'-precipitates of 51% with an average dimension of 0.5μm, and a channel width of 125nm.

Tensile specimens from the three corners of the stereographic triangle were machined from the slab using wire electron discharge machine (EDM). The expected orientations of the specimens are given in Table 1. Specimens of a particular loading orientation were cut parallel to each other so that the Laue back-reflection x-ray diffraction could be performed on one specimen for each orientation. Laue results indicated that all expected orientations were off by no more the 8 degrees. The specimens were designed as flat dogbones, 32mm long, with a gage length of 17mm, and width and thickness of 3.0mm and 1.60mm respectively. The <111> oriented specimens were shorter than the <100> or <110> loaded specimens due to the dimensions of the slab. The <111> oriented specimens were 23 mm long, with a gage length of 9.2mm, and the width and thickness of 2.5mm and 2.0mm, respectively. In order to remove the damaged material on the surface from the EDM process, the specimens were mechanically polished as well as electro-polished to the final dimensions on their faces as well as sides.

Tensile testing was conducted at room temperature and at the nominal strain rate of $10^{-5}s^{-1}$. The elastic portions of the stress-strain curves are not accurate since the strain values have been calculated from the crosshead speed and not using an extensometer in

an effort to limit the interference with slip-trace analysis. One specimen from each orientation was loaded to fracture while a second specimen from each orientation was loaded to different strain levels in order to study the development of slip bands. Optical and scanning electron microscopy techniques were used to study the slip traces of the specimens. All micrographs are displayed with the loading axis parallel to the vertical direction.

### 3. Results

#### *3.1 Stress-Strain Curves*

Figure 2 shows the engineering stress-strain curves for the orientations of interest, which were all calculated from specimens loaded to fracture. A summary of the tensile results is presented in Table 2. The stress-strain curve for the $[1\bar{1}0]$ oriented specimens showed a distinct upper and lower yield point, which was maintained until fracture. Specimens oriented with the loading axes of $[100]$ and $[1\bar{1}1]$ did not show an upper and lower yield point but the load at which yielding occurred was well-defined. The average CRSS calculated based on octahedral slip systems from the yield stress of $[100]$ and $[1\bar{1}0]$ oriented specimens showed an approximately 10MPa difference, which is within the expected range of error. However, the $[1\bar{1}1]$-oriented specimens showed an average CRSS of 248MPa, which is approximately 120MPa below the values for the other two orientations. The finding of a lower CRSS for the <111> oriented samples is consistent with previously reported results for Ni-base superalloys of similar microstructure [2,15]. Although the activation of the {100} slip planes at room temperature is not expected, the CRSS for these slip systems were also calculated. As shown in Table 2, the $[1\bar{1}1]$

oriented specimens showed the highest CRSS when resolved on the cube slip system and was approximately 100MPa higher than the value for the [1 $\bar{1}$ 0]-oriented sample.

### 3.2 Deformation at Yielding

Figure 3 shows the traces observed using optical microscopy on the face and the side of the [1 $\bar{1}$ 0]-oriented specimen loaded to 0.88% plastic strain. The thinner traces were somewhat straight and relatively sharp, however, they branched moderately in the thicker bundles. Figure 3a illustrates the possible slip traces for this loading orientation. Both the face and the side traces matched the expected octahedral slip lines of 90° (angles are defined relative to the loading axis) on the face (shown in Figure 3b) corresponding to slip on the (111) or (11 $\bar{1}$) planes and two sets of 54° traces on the side corresponding to slip occurring on the (111) and (11 $\bar{1}$), respectively, as seen in Figure 3c. The traces were difficult to find and appeared differently when studied using SEM as depicted in Figure 4. Detailed investigations in the SEM revealed that the surface topography that resulted in the observation of traces in the optical microscope was not the typical displacement of the surface along the direction of the activated Burgers vectors. The traces were associated with a change in the channel size and, as shown at high magnification in Figure 4b, some of the $\gamma$' cubes were actually pushed out and left a hole in the structure. Further observations of the [1 $\bar{1}$ 0]-oriented specimen revealed evidences of particle shearing within the traces as shown in Figure 4c. The correspondence of the slip lines among several precipitates indicates that the slip also occurred through the $\gamma$-matrix. Figure 5 demonstrates how the deformation process was achieved through the movement of a Lüders band, which formed at one end of the specimen, and correlates with the upper and lower yield points observed after .88% plastic strain. The dark shadow observed in Figure

5 is due to the ripples on the surface of the sample caused by the bending moment created by the propagation of the Lüders band. Also, it is important to note that near the shoulder of the samples, where the stress state is triaxial, the traces followed curved paths, not corresponding to the expected octahedral slip planes.

The traces observed on both surfaces of the [100]-oriented specimen loaded to 0.2% strain, as shown in Figure 6b and 6c, were approximately at 60° on the face and at 45° on the side of the sample, which did not match any of the possible slip traces - cube or octahedral – as shown in Figure 6a. Interestingly, only one set of traces was observed on each surface, although one would have expected multiple slip plane activation in a <100> loaded crystal. Based on the angles of the traces on the face ((011) plane) and on the side (($0\bar{1}1$) plane) the apparent slip plane should be close to that of a {331} plane. Furthermore, the traces observed in this orientation were not as distinct as those found on the surfaces of the [$1\bar{1}0$] oriented specimens. They were more wavy and thicker with significant off branching from one trace to another. No particle shearing was detected within the bundles at this strain level.

Figure 7a depicts the possible slip traces for the [$1\bar{1}1$] loading orientation. The traces observed on both surfaces of the [$1\bar{1}1$]-oriented specimen loaded to 0.9% plastic strain are given in Figures 7b and 7c. Figure 7b illustrates that two sets of traces were observed on both surfaces of the sample. The traces observed on the face (Figure 7b) sit at approximately 55° and 35° angles. The 55° traces are relatively localized but wavy, and appear to form in bundles, densely grouped together. The second set of traces on the face, which formed at 35°, was relatively sharp and not as pronounced. Similarly, the 90° traces produced on the side of these samples were very wavy while the 39° traces were

relatively sharp and distinct as shown in Figure 7c. The two sets of traces observed on the face and the sides of the [1 $\bar{1}$ 1] oriented sample match the predicted traces for the cube slip system as shown in Figure 7a. This behavior is consistent with the reported cube slip traces in the <111> oriented Ni-base superalloys tested at 650°C and 750°C [14]. Similar to the [100]-oriented sample, no particle shearing was observed within the deformation bands at this applied strain level.

### 3.3 Deformation behavior beyond yielding

The [1 $\bar{1}$ 0]-oriented specimens behaved differently from the, [100] or the [1 $\bar{1}$ 1] specimens, and exhibited no strain hardening. As previously mentioned, these specimens deformed through the propagation of a Lüders band. However, the band never traveled the entire length of the specimen prior to fracture, which explains why the flow stress never increased with strain. Figure 8 illustrates the traces observed on the side of an [1 $\bar{1}$ 0]-oriented specimen near the fracture surface. As far as the orientation of the slip traces are concerned, they match those observed at yielding (i.e. traces of {111} planes), however they are sharper, thinner and denser.

The [100]-oriented specimens continued to show traces similar to those observed at yielding except near the fracture surface, where very sharp, fine and delineated traces, which their angles match those expected by slip on the octahedral planes, were observed as shown in Figure 9. Figure 9b demonstrates that within these regions, the γ' particles are sheared.

Similar to the behavior exhibited in the [100]-orientated samples, octahedral slip traces were also observed in the [1 $\bar{1}$ 1]-oriented specimens near the fracture surface as shown in Figure 10a. Again in these regions, the slip lines are very straight, fine and

delineated. As shown in Figure 10b, the observation of these slip lines is also associated with extensive particle shearing.

## 4. Discussion

Three points are evident from the above results; one that the Ni-base alloy tested in this study does not follow Schmid law, second that the macroscopic deformation traces observed on the surfaces of samples are quite wavy and do not correspond to the expected slip bands (except for the $[1\bar{1}0]$-oriented sample), and third that near fracture surfaces, where the strain levels are high, all three orientations studied show straight and sharp slip lines, corresponding to the octahedral slip and associated with γ'-particle shearing. Furthermore, it was demonstrated that the wavy deformation traces observed on the surfaces at low magnifications in optical microscope correspond to local changes in the channel size and the falling off of the γ'-precipitates as viewed at high magnifications in the SEM.

At room temperature the γ'-phase has a relatively low CRSS and the relative channel width and the γ/γ' interfacial structure/chemistry govern the yielding process [9]. Since the average channel size in the γ/γ' microstructure tested here is relatively large (125nm), it is anticipated that yielding was initiated by the bowing of dislocations in the γ-matrix channels rather than by the independent plastic deformation of the γ'-particles. We suggest that the confinement of dislocation motion in between the γ-channels is responsible for the change in the channel width and the expelling of the γ'-particles on the surface, which result in the observation of deformation traces. Plastic localization was observed in samples of all three orientations and consistent with previously reported

results [16], the degree of deformation localization increased in the order of <111>, <100> and <110> orientations. The questions to be answered are why the path of deformation is so localized and why it varies among the three crystallographic orientations tested. For the $[1\bar{1}0]$ orientation, the deformation traces matched the predicted octahedral slip traces, the $[1\bar{1}1]$-oriented samples exhibited deformation traces that corresponded to the cube slip system, whereas the traces did not match neither octahedral or cube slip traces for samples tested in the [100] orientation.

As stated by Österle et al. [11], in Ni-base superalloys, the probability of cross-slip among the {111} planes is expected to play an important role on the expansion of the dislocation loops in the $\gamma$-channels. While the fine deformation structure depends on the probability of cross-slip, the meso- and macro-scale has been found to be similar in precipitation hardened face centered cubic (FCC) alloys with vastly different cross-slip ability [17]. We propose that in addition to the effect of cross-slip probability based on the crystallographic orientation, the development of localized shear stresses at various levels – macroscopic and mesoscopic – significantly affect the deformation path in single crystal superalloys. Two paths govern the general course of strain localization, paths of maximum resolved shear stress and locations of minimum resistance to shear. Macroscopically, during uniaxial loading of isotropic materials, maximum shear stresses develop on planes located at 45° relative to the loading axis. However, the orientation of the maximum shear stress planes varies depending on the elastic and/or plastic anisotropy as well as the stress state [18]. As far as response of the material to shear stress is concerned, there is a broad range of behaviors that may lead to plastic strain localization, as reviewed by Luft [19]. Low local strain-hardening rate and low strain rate sensitivity

encourage localization, and when their values become negative they may cause tensile plastic instability. In superalloys, the γ'-particle shearing is a recognized mechanism for work softening, however our results indicate that at least in the <100>- and <111> oriented samples no particle shearing occurred within the deformation tarces. In single crystals, shear bands can also form with positive work hardening rate without any of the microstructural weaknesses that causes work-softening. This comes about when non-Schmid effects are included in the description of yielding as recognized and discussed by Asaro and Rice [20]. Coarse slip bands also develop based on the same principles [21] and their clustering results in the formation of macroscopic shear bands [22]. Detailed analysis is required to understand the contribution of these phenomena, which modify the local resolved shear stress values on the slip systems, to the observed deformation paths.

Mesoscopically, any discontinuity in the structure, such as presence of pores and eutectic pools will also create localized tri-axial stresses. When the distance between the discontinuities is short enough, the strain fields around each will begin to overlap and interact. The interaction between their strain fields produces a maximum shear stress path dictated by the position of the pores or eutectic pools. Within these localized paths, due to stress intensification, the resolved shear stresses achieved on the octahedral planes will also be higher. In this study, detailed examination revealed localized deformation occurring at such features as demonstrated in Figure 11 for the samples loaded in the $[1\bar{1}1]$ direction. To demonstrate the effect of these discontinuities on the yielding process, a sample was loaded in the elastic limit to 70% of its yield strength. As shown in Figure 11b, areas of localized yielding were detected near the pores. The association of a higher density of pores in the regions of localized deformation can also be detected in

Figure 7. For the [1 1̄ 0]-loaded samples, which showed relatively straight deformation traces, no correlation between the geometrical arrangement of pores (or eutectics) and slip localization was found. The observation of severely localized slip bundles that correspond to the activation of the octahedral slip planes in the [1 1̄ 0]-loaded samples is attributed to the limited cross-slip among the {111} slip planes [23], which results in the pile-up of dislocation at the γ/γ' interface, and hence shearing of the γ'-particles at relatively low strain values (see Figure 4c). It should be noted that, as demonstrated in Figure 5, near the shoulder, where the triaxial stress-state causes the activation of other slip systems, the deformation path becomes wavy because of the increases in possibility of cross-slip among the activated slip planes. This observation confirms that if extensive cross-slip is probable, the deformation will meander among the γ-channels and the path would depend on the macroscopic stress field, rather than the expected slip traces.

The pores and eutectic pools develop during the solidification process of single crystal superalloys at the inter-dendritic positions, approximately along the <100> directions. The differences in the CRSS and in the deformation behavior between the [1 1̄ 1]-loaded and the other two tested orientations may be associated with the differences in the relative geometry of these stress raisers. In the [100]-loaded samples, the deformation traces appeared less localized but more wavy than the [1 1̄ 1]-oriented samples and with no grouping of the deformation bundles (compare Figures 6 and 7), suggesting that the strain localization between pores (or eutectics) played a less significant role in the former orientation. Consistently, for this orientation, the observed deformation traces were not the same as those would have been formed by localization at the mesoscopic level on the (011) or (01 1̄) plane. In the <111>-loaded samples, the

pores (or eutectics) are equally distributed at approximately 54° relative to the loading axis and with the shortest distance in between them. The shorter the distance between the discontinuities the higher is the probability of the overlap of their stress fields. Considering that no particle shearing was observed in the [1 $\bar{1}$ 1]-oriented sample (except near the fracture region), it is suggested that the lower critical resolved shear stress calculated for this orientation is mainly due to the stress localization and intensification at a mesoscale, i.e. in between the microstructural discontinuities. The stress intensification results in a lowering of the remote applied stress needed to achieve CRSS on {111} planes. Further work is in progress to understand the evolution of dislocations within the deformation traces as a function of the loading orientation and test temperature.

The strain hardening behaviors of the samples (see Figure 2) also reflect their deformation processes. In the [1 $\bar{1}$ 0]-oriented samples, the γ'-particles were sheared and caused intense localization on a single slip system due to local softening, which resulted in the observation of the upper- and lower- yield points, development of Lüders band and lack of strain hardening. The plastic deformation of the [100]-oriented samples proceeded by the development of one set of deformation traces. It should be noted that this does not mean that only one slip system was activated, it only indicates that macroscopic localization occurred in this orientation. Considering the mechanism suggested for the zig-zag deformation within the γ-channels by Österle et al. [11], the observed strain hardening arose from the interaction of dislocations, on possibly two octahedral slip planes, within the deformation band. The [1 $\bar{1}$ 1]-oriented samples showed initially a relatively low strain hardening rate and with increasing strain beyond approximately 3%, the strain hardening rate increased significantly, and then decreased again. This behavior

is superficially similar to the deformation of FCC crystals oriented for easy glide. The deformation of these samples proceeded by the development of two sets of deformation traces. The high strain hardening may be attributed to the interaction among the intersecting dislocation paths. Indeed as demonstrated in Figure 7a, the propagation of one deformation band is interrupted by intersection with the second band. Of course, with increasing the stress level, cross-slip rate among {111} planes becomes higher and the strain hardening rate decreases.

The fracture of all samples proceeded by necking, $\gamma'$-particle shearing and the observation of fine sharply defined slip traces on octahedral slip planes. In the $[1\bar{1}0]$ oriented sample, where particle shearing began at low strain levels and deformation was limited to a single slip system, fracture occurred when noticeable deformation on a second slip system was initiated. Similar behavior has been observed in the case of Ni-base superalloys that deform by easy glide [23].

## 5. Conclusions

The evolution of deformation in tensile specimens of a $\gamma/\gamma'$ superalloy oriented in <100>, <110> and <111> orientations was investigated. The results of this study lead to the following conclusions:

1. Plastic deformation within $\gamma$-channels causes changes in the channel width and falling off of the $\gamma'$-particles on the surface, which result in the observation of "deformation traces". These deformation traces are wavy and do not necessarily correspond to the predicted octahedral slip traces. Their paths depend on the complex interaction between strain localization mechanisms at macroscopic, meoscopic and microscopic levels.

2. The dependency of the deformation behavior on the loading direction is associated with the cross-slip probability as well as the relative orientation of the dendrites. There is a low probability of cross-slip in the <110>-oriented samples, therefore plastic deformation proceeds by deformation on one slip system, which results in $\gamma$'-particle shearing and low strain hardening rate. The deformation in the <111>-oriented samples is dominated by the localized deformation between the pores and eutectic pools that deform in between the dendrites. In the <100>-oriented samples the influence of the interdendritic features is less prominent due to their orientation and spacing relative to the macroscopic maximum shear stress planes.

3. The lower CRSS of the <111>-oriented samples may be attributed to the strain localization at a mesoscopic level, which results in the development high local shear stresses.

4. Under the conditions of large strains or low probability of cross-slip, $\gamma$'-particles are sheared and the observed deformation traces correspond to the octahedral slip systems. The presence of triaxial stresses retards the probability of particle shearing by increasing the probability of cross-slip among the {111} planes and cause the observation of wavy deformation traces.

## 6. Acknowledgements

# References

1. R.V. Miner, R.C. Voigt, J. Gayda, and T.B. Gabb, Metallurgical Transaction , 17A, 491-496, 1986.
2. D.M. Shah, D.N. Duhl, in Superalloys '84, ed M. Gall et al. ASM, Metals Park, p. 105, 1984.
3. R. V. Miner, Metall. Mater. Trans. A, 28, 1011, 1997.
4. M. Nazmy, A. Kunzler, J. Denk and R. Bauman, Scripta mater., 47, 521, 2002.
5. C. Lall, S.Chin, D.P. Pope, Metallurgical Transactions A, 10A, 1323, 1979.
6. V. paidar, D. P. Pope and V. Vitek, Acta metal. 32, 435, 1984.
7. A. Aoki and O. Izumi, Acta metal. 26, 1257, 1978.
8. T. M. Pollock and A. S. argon, Acta metal. mater., 40, 1, 1992.
9. M.Feller-Kneipmeier, T. Link, I.Poschmann, G. Scheunemann-Frerker, C. Schulze, Acta Mater, 44, n6, 2397-2407, 1996.
10. A. Nitz, U. Lagerpusch, E. Nembach, Acta mater, 46, n13, 4769-4779, 1998.
11. W. Österle, D. Bettge, Fedelich, H. KlingelÖffer, Acta Mater, 48, 689-700, 2000.
12. A. Nitz, E. Nembach, Materials Science & Engineering A234, 684-686, 1997.
13. R.V. Miner, T.B. Gabb, J. Gayda, and K. J. Hemker, Metallurgical Transaction A, 17, 507, 1986.
14. D. Bettge, W.Österle, Scripta Materialia, 40, n4, 389-395, 1999.
15. F. E. Heredia and D. P. Pope, Acta metal., 34, 279, 1986.
16. X. Wu, J. H. Zhang, J. L. Liu, T. Jin, Y. B. Xu and Z. Q. Hu, Mater. Sci. Eng. A, 325, 478, 2002.
17. A. Ziegenbein, Ch. Achmus, J. Plessing and H. Neuhäuser, in *Plastic and Fracture Instabilities in Materials*, ASME Materials Division, **200** (1995) 101-118.
18. W. A. Backenhofen, Metall.Trans, 4, 2682, 1973.
19. A. Luft, *Prog. Mater. Sci.*, **35** (1991) 97-204.
20. R. J. Asaro and J. R. Rice, *Journal of the Mechanics and Physics of Solids*, **25** (1977) 309-338.
21. Y. W. Chang and R. J. Asaro, Acta metal., 29, 241, 1981.
22. M. Dao and R. J. Asaro, Scripta metal. Mater., 30, 791, 1994.
23. L.P. Kubin, B. Lisiecki, P. Caron, Philisophical Magazine A, 71, n5, 991-1009, 1995.
24. F. Ebrahimi, J. Yanevich and D.P. Deluca, Acta Mater, 48, 469-479, 2000.

Table 1. Loading, face, and side orientations of dog-bone shaped specimens tested in this study.

| Loading | [1 $\bar{1}$ 1] | [1 $\bar{1}$ 0] | [100] |
|---|---|---|---|
| Face | [011] | [001] | [011] |
| Side | [21 $\bar{1}$] | [110] | [0 $\bar{1}$ 1] |

Table 2. A summary of tensile properties.

| Approx Loading Axis | Yield Stress (MPa) | CRSS (Octahedral system) (MPa) | CRSS (Cube system) (MPa) | $\varepsilon_{plastic}$ | UTS (MPa) |
|---|---|---|---|---|---|
| 100[a] | 876 | 357.6 | ----- | 12.0 | 1140 |
| 100[b] | 866 | 353.5 | ----- | 0.3* | ----- |
| 1$\bar{1}$0[a] | 908 | 370.7 | 321 | 35.5 | 857 |
| 1$\bar{1}$0[b] | 922 | 376.4 | 326 | .88* | ----- |
| 1$\bar{1}$1[a] | 914 | 248.7 | 430 | 14.0 | 1548 |
| 1$\bar{1}$1[b] | 895 | 243.5 | 422 | .9* | ----- |

[a] – Loaded to fracture.
[b] – partially loaded.
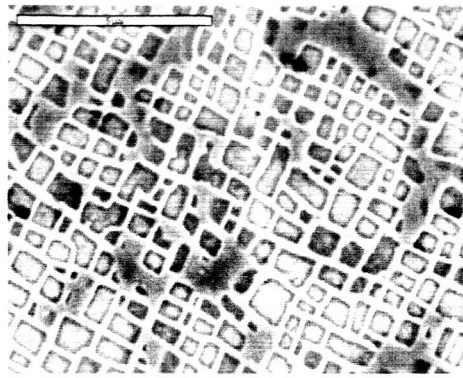
Figure 1. SEM micrograph showing the microstructure of the superalloy studied.
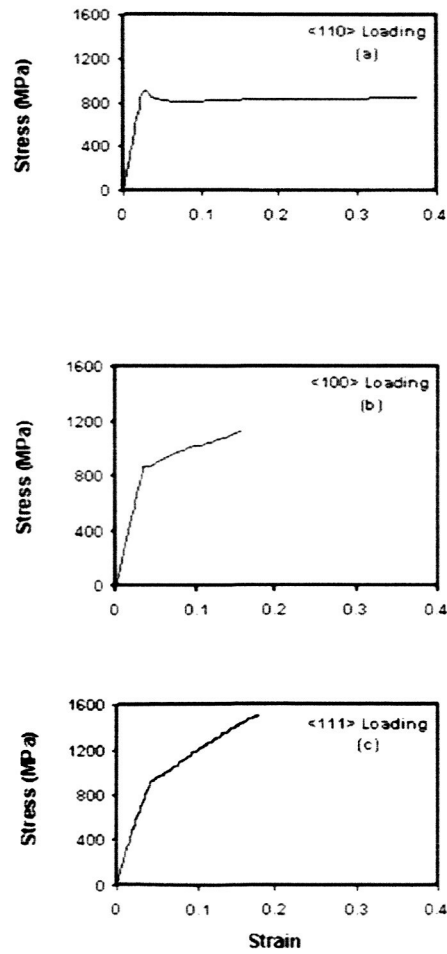


Figure 2. Tensile stress-strain curves for the three orientations tested.
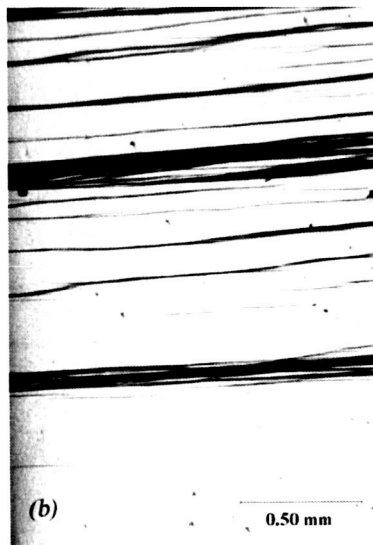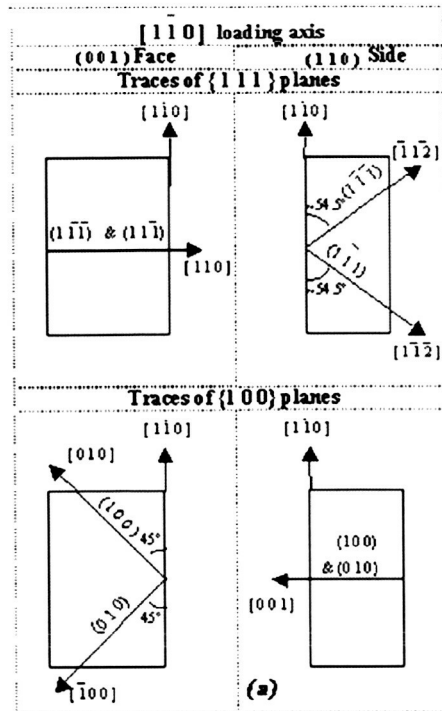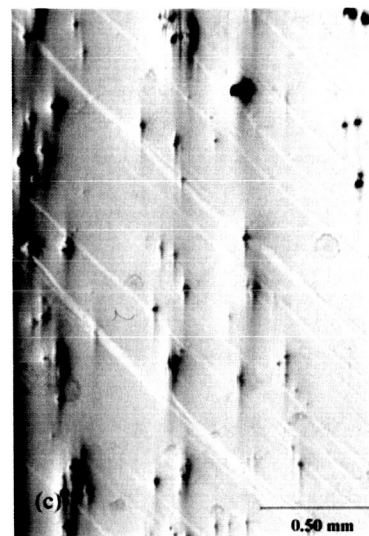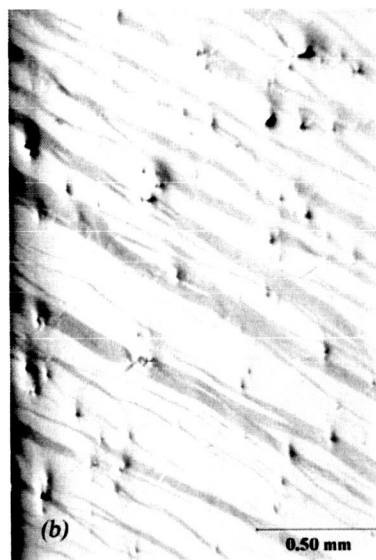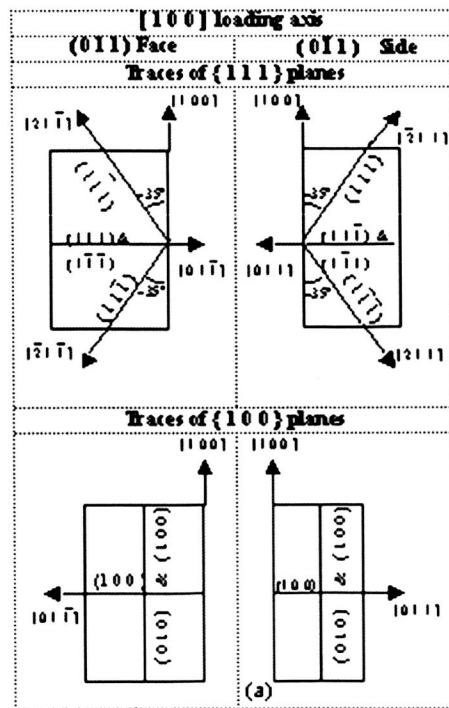
Figure 3. (a) The expected slip traces for octahedral and cube slip systems for the [1 $\bar{1}$ 0] loading orientation. Optical micrographs showing deformation bands matching the traces of (111) and (11 $\bar{1}$) planes (a) at 90° on the face and (b) at 54° on the sides of a sample loaded to 0.88% plastic strain.
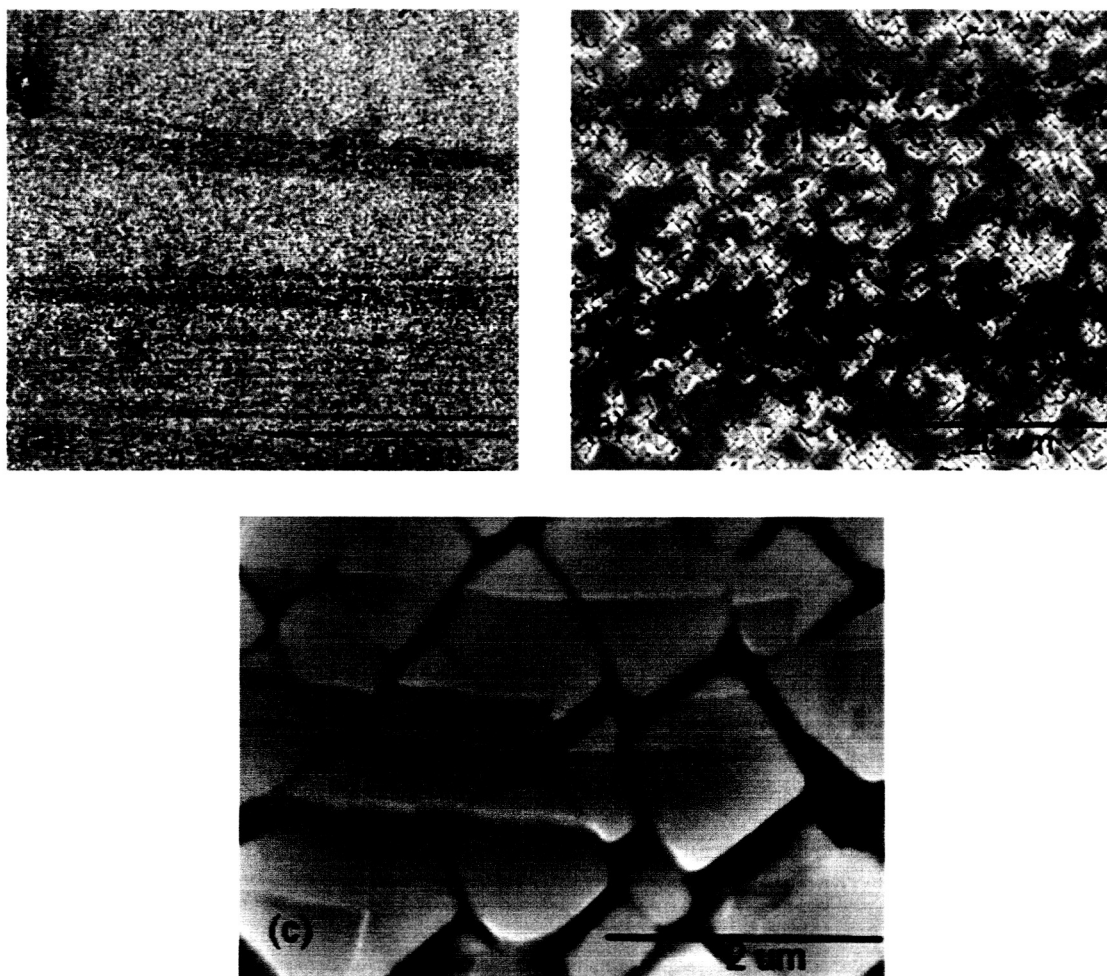
Figure 4. SEM micrographs showing (a) the deformation traces at a low magnification, (b) the change in the $\gamma$-channel width and falling-off of $\gamma'$-particles within traces, and (c) $\gamma'$-particle shearing within the deformation bands in the [1 $\overline{1}$ 0]-loaded sample.



Figure 5. A low magnification optical montage showing the inhomogeneous deformation in the [1 $\overline{1}$ 0]-loaded sample. Note the angle and waviness of the slip traces near the shoulder of the sample.

Figure 6. (a) The expected slip traces for octahedral and cube slip systems for the [100] loading orientation. Optical micrographs showing deformation bands (a) on the (011) face at approximately 60° and (c) on the (0$\bar{1}$1) side at approximately 45° in a sample loaded to 0.2% plastic strain. Note that the deformation bands do not match octahedral or cube slip systems.
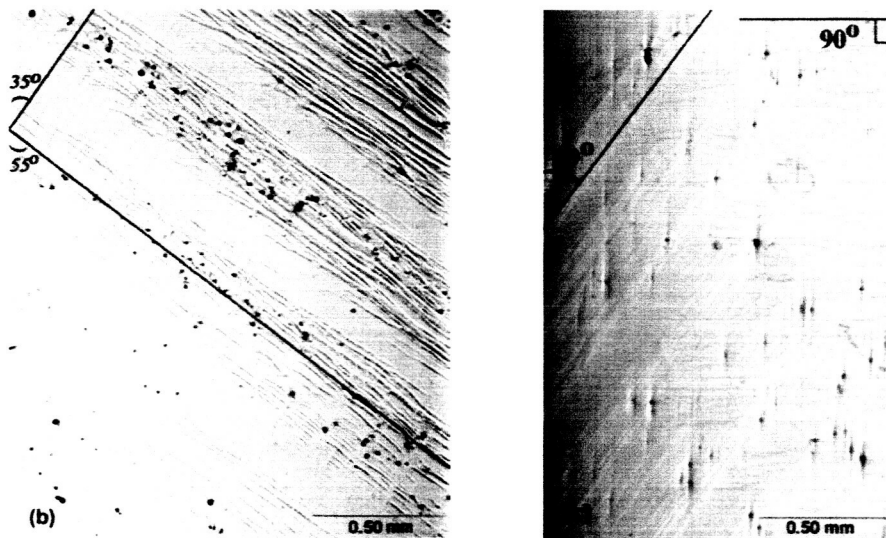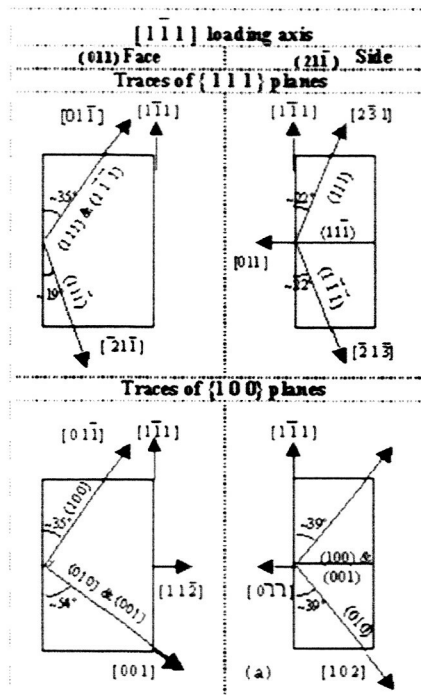
Figure 7. (a) The expected slip traces for octahedral and cube slip systems for the $[1\bar{1}1]$ loading orientation. Optical micrographs showing deformation bands (b) on the (011) face and (c) on the $(21\bar{1})$ side of a sample loaded to 0.9% plastic strain. Note that the deformation bands match the traces predicted for cube slip.

Figure 8. Optical micrograph showing the development of sharp and dense slip bands on the side surface of a $[1\bar{1}0]$-oriented sample loaded to fracture.
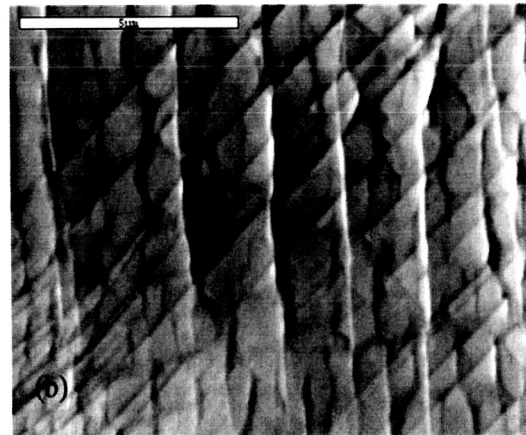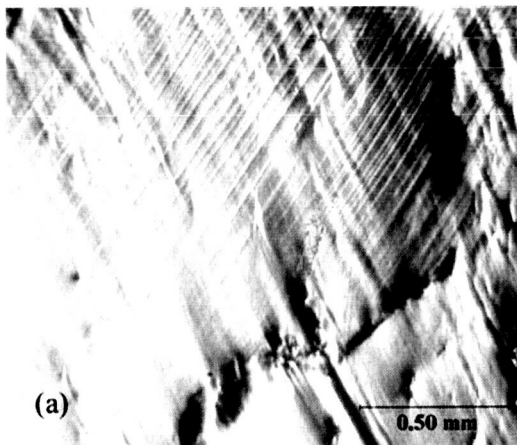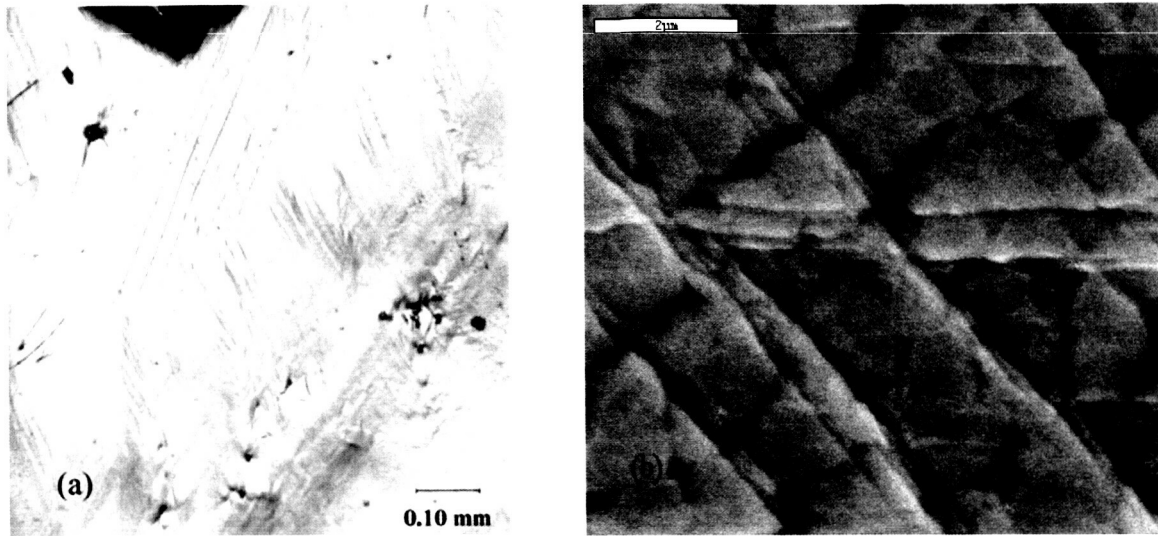


Figure 9. (a) Optical micrograph showing the development of sharp and dense slip bands matching the predicted slip traces for octahedral slip at approximately two 35° angles on the face of a [100]-oriented sample loaded to fracture. (b) SEM micrograph illustrating $\gamma$'-particle shearing within the slip bands.

Figure 10. (a) Optical micrograph showing the development of sharp and dense slip bands matching the predicted slip traces for octahedral slip at approximately 35° and 19° angles on the face of a [1 $\bar{1}$ 1]-oriented sample loaded to fracture. (b) SEM micrograph illustrating γ'-particle shearing within the slip bands.
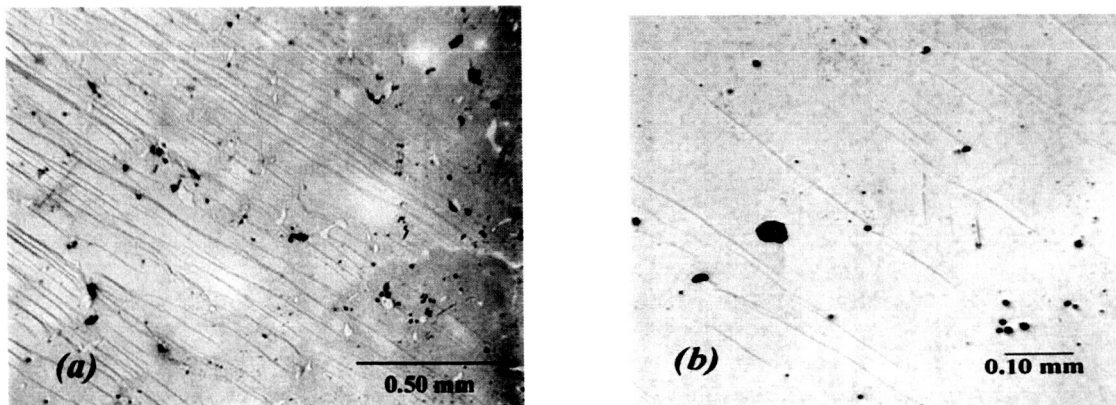


Figure11. Optical micrograph showing slip-pore interaction in samples loaded to (a) yield stress and (b) 70% of the yield stress along the [1 $\bar{1}$ 1] direction.